






## Article

# JNK Signalling Regulates Self-Renewal of Proliferative Urine-Derived Renal Progenitor Cells via Inhibition of Ferroptosis

Lisa Nguyen <sup>1</sup>, Leonie Thewes <sup>2</sup>, Michelle Westerhoff <sup>3</sup>, Wasco Wruck <sup>1</sup>, Andreas S. Reichert <sup>3</sup>, Carsten Berndt <sup>2</sup> and James Adjaye <sup>1,4,\*</sup>

- <sup>1</sup> Institute of Stem Cell Research and Regenerative Medicine, University Hospital Düsseldorf, Medical Faculty, Heinrich-Heine University Düsseldorf, 40225 Düsseldorf, Germany; lisa-nguyen@med.uni-duesseldorf.de (L.N.); wasco.wruck@med.uni-duesseldorf.de (W.W.)
- <sup>2</sup> Department of Neurology, University Hospital Düsseldorf, Medical Faculty, Heinrich-Heine University Düsseldorf, 40225 Düsseldorf, Germany; leonie.thewes@uni-duesseldorf.de (L.T.); carsten.berndt@uni-duesseldorf.de (C.B.)
- <sup>3</sup> Institute of Biochemistry and Molecular Biology I, University Hospital Düsseldorf, Medical Faculty, Heinrich-Heine University Düsseldorf, 40225 Düsseldorf, Germany; michelle.westerhoff@hhu.de (M.W.); reichert@hhu.de (A.S.R.)
- <sup>4</sup> EGA Institute for Women's Health, Zayed Centre for Research into Rare Diseases in Children (ZCR), University College London (UCL), 20 Guilford Street, London WC1N 1DZ, UK
- \* Correspondence: james.adjaye@med.uni-duesseldorf.de

**Abstract:** With a global increase in chronic kidney disease patients, alternatives to dialysis and organ transplantation are needed. Stem cell-based therapies could be one possibility to treat chronic kidney disease. Here, we used multipotent urine-derived renal progenitor cells (UdRPCs) to study nephrogenesis. UdRPCs treated with the JNK inhibitor—AEG3482 displayed decreased proliferation and downregulated transcription of cell cycle-associated genes as well as the kidney progenitor markers—SIX2, SALL1 and VCAM1. In addition, levels of activated SMAD2/3, which is associated with the maintenance of self-renewal in UdRPCs, were decreased. JNK inhibition resulted in less efficient oxidative phosphorylation and more lipid peroxidation via ferroptosis, an iron-dependent non-apoptotic cell death pathway linked to various forms of kidney disease. Our study is the first to describe the importance of JNK signalling as a link between maintenance of self-renewal and protection against ferroptosis in SIX2-positive renal progenitor cells.

**Keywords:** JNK signalling; urine stem cells; self-renewal; ferroptosis; cell death; mitochondrial metabolism



**Citation:** Nguyen, L.; Thewes, L.; Westerhoff, M.; Wruck, W.; Reichert, A.S.; Berndt, C.; Adjaye, J. JNK Signalling Regulates Self-Renewal of Proliferative Urine-Derived Renal Progenitor Cells via Inhibition of Ferroptosis. *Cells* **2023**, *12*, 2197. <https://doi.org/10.3390/cells12172197>

Academic Editor: Pei-Hui Lin

Received: 18 July 2023

Revised: 25 August 2023

Accepted: 31 August 2023

Published: 2 September 2023



**Copyright:** © 2023 by the authors. Licensee MDPI, Basel, Switzerland. This article is an open access article distributed under the terms and conditions of the Creative Commons Attribution (CC BY) license (<https://creativecommons.org/licenses/by/4.0/>).

## 1. Introduction

Due to the increasing level of patient mortality due to kidney-associated diseases, new medical options besides the conventional dialysis and organ transplantation are needed. However, shortage of donor organs and immune compatibility restrict these therapeutic approaches. A future therapy option may be cell replacement therapies with pluripotent stem cell (PSC)-derived cellular products; however, these have drawbacks that include ethical concerns and tumorigenicity. A counter measure to the use of PSCs is the use of cost-effective and non-invasive urine cells. Cell types isolated from urine include urine stem cells, podocytes and proximal tubule epithelial cells [1]. Highly interesting for research and medical purposes is the subpopulation of multipotent urine stem cells (USCs) which display typical MSC characteristics [2–5]. Besides expressing kidney-specific markers such as podocin and synaptopodin [3,4], USCs express the renal progenitor marker sine oculis homeobox homolog 2 (SIX2). Based on SIX2 expression, we conveniently coined the term urine-derived renal progenitor cells (UdRPCs) [2]. Presumably, UdRPCs originate from the

upper urinary tract of the kidney, which was indicated by the presence of Y chromosomes in these cells, isolated from the urine of a female patient who received a kidney transplant from a male donor [6].

The proliferative potential of UdrPCs and their ability to differentiate into various kidney cell types, such as podocytes [7] and tubular cells (unpublished), make them a promising tool for kidney regeneration experiments. Results from our earlier study suggested the maintenance of self-renewal of UdrPCs via FGF and TGF $\beta$  signalling with modulations of JNK signalling [2]. JNK is part of the mitogen-activated protein kinase (MAPK) family and each pathway is a sequential activation of MAPKKs [8]. This pathway is involved in various processes such as proliferation and survival as well as stress and inflammation-induced apoptosis and is also linked to acute and chronic kidney diseases [9–12]. In nephron progenitor cells, JNK signalling plays a major role in maintaining the progenitor fate.

In recent decades, the cellular process of ferroptosis was discovered to play a role in the emergence of kidney diseases [13]. Ferroptosis was named in the article by Dixon et al. [14] in 2012 as an iron-dependent form of non-apoptotic cell death. It is characterised by accumulation of iron that leads, in combination with peroxides, to lipid peroxidation [15,16]. Glutathione peroxidase 4 (GPX4) catalyses the glutathione (GSH)-dependent reduction of H<sub>2</sub>O<sub>2</sub> and hydroperoxides of polyunsaturated fatty acids to the corresponding alcohols, thus restricting the cellular levels of peroxides and repairing oxidised lipids [17,18]. A depletion of glutathione levels and a consequent decrease in GPX4 activity leads to the accumulation of lipid peroxidation and subsequently to membrane destruction [17,19]. Other circumstances, such as activated mitochondrial voltage-dependent anion channels and mitogen-activated protein kinases, stress on endoplasmic reticuli and inhibited cystine/glutamate antiporters, may also induce ferroptosis [15,19]. Ferroptosis-induced morphology changes include blistered cell membrane, lack of chromatin condensation, fewer and more fragmented mitochondria with denser membranes and reduction or disappearance of cristae [15,17]. Thereby, ferroptosis is involved in various diseases of the brain, heart, liver and kidney [17,20]. Studies on mice demonstrated a lack of fully functional GPX4, a key suppressor of ferroptosis, resulting in acute kidney failure [21,22]. Besides acute kidney failure, ferroptosis-induced diseases in the kidney include acute kidney injury, I/R injury, clear cell renal cell carcinoma and adrenocortical carcinomas [17].

For this study, we investigated the effects of JNK signalling on three different UdrPC cultures by applying the inhibitory compound AEG3482 for 72 h. We were able to connect JNK signalling with the maintenance of proliferation and self-renewal in UdrPCs. Moreover, JNK inhibition induced ferroptosis and reduced cellular oxidative phosphorylation via disruption of the mitochondrial membrane potential. We propose that UdrPCs treated with a JNK inhibitor can be used for modelling ferroptosis-induced kidney diseases and promotion of JNK signalling in UdrPCs may represent a novel strategy for kidney regeneration experiments.

## 2. Materials and Methods

### 2.1. Cell Culture

For this study, three distinct UdrPC lines, UM51, UM27 and UF21, were used. Their names describe the donor's gender (UM—urine male; UF—urine female) and age. The cells were cultivated on 0.2% gelatine-coated plates and were maintained in proliferation medium supplemented with 5 ng/mL bFGF (Peprotech) every second day [2]. The optimal concentration of the JNK inhibitor AEG3482 (TOCRIS, EC<sub>50</sub> = 20  $\mu$ M) was determined by titration of different concentrations on UM51 cells. The concentrations 10  $\mu$ M, 50  $\mu$ M and 100  $\mu$ M of AEG3482 inhibitor were applied to UM51 cells for 48 h to 120 h with daily medium change. A concentration of 10  $\mu$ M of AEG3482 was adopted for subsequent experiments. At 80% confluency, cells were trypsinised with TrypLE (Life Technologies, Carlsbad, CA, USA) and were seeded on gelatine-coated plates. The treatment with 10  $\mu$ M AEG3482 inhibitor was started at 60–70% confluency and was maintained for 24 h, 72 h

and 120 h. In parallel, untreated cells were kept as controls for the same time points and were cultivated in proliferation medium with daily medium changes. Like UM51 cells, the cell lines UM27 and UF21 were treated for 72 h with 10  $\mu$ M JNK inhibitor AEG3482 with daily medium changes.

## 2.2. siRNA Transfection

Estimation of the needed siRNA concentration was carried out in UM27 cells. The concentrations 250 ng, 500 ng and 1000 ng of siJNK (Sigma-Aldrich, St. Louis, MO, USA; s: GUUCUUAUGAAAUGUGUUA[dT][dT], as: UAACACAUUUCAUAAGAAC[dT][dT]) were transfected twice, with 48 h intervals between the transfections. Scrambled siRNA (Sigma-Aldrich) of the same concentrations was used as a control. The concentration of 1000 ng of siJNK was used for further transfections. In short, nanoparticle complexes were prepared by adding Xfect Polymer (Takara, Shiga, Japan) to Xfect Reaction Buffer (Takara) containing the siRNAs and incubating the solution for 10 min at RT. The entire solution was added dropwise to the wells and gently mixed, before overnight incubation at 37 °C and 5% CO<sub>2</sub>. The medium was refreshed the next day and the transfection was repeated after 48 h. Protection from lipid peroxidation was tested by addition of 100 nM of the ferroptosis inhibitor liproxstatin-1 (Lip-1) 1 h prior to transfection and continued supplementation in the medium.

## 2.3. Proliferation Assay

After JNK inhibition, cells were fixed with 4% paraformaldehyde (Polysciences, Warrington, PA, USA) and stained with the antibody anti-mouse KI67, 1:200 (CST). Randomly chosen pictures were taken from each well and KI67-positive cells as well as total cell numbers were counted (N = 10). The ratio of KI67-positive/total cell number was calculated and statistical analysis was processed in GraphPad Prism software 8.0.2 (Dotmatics, Boston, MA, USA). *p*-values were calculated with an unpaired *t*-test (two-tailed) (\* *p*-value < 0.05, \*\* *p*-value < 0.01, \*\*\* *p*-value < 0.001).

## 2.4. Flow Cytometry-Based Measurement of Cell Death

JNK-inhibited cells and the respective controls were washed twice with PBS and further stained with 10  $\mu$ g/mL propidium iodide (PI) (Invitrogen, Waltham, MA, USA) for 15 min at 37 °C and 5% CO<sub>2</sub>. After two washing steps with PBS, the cells were harvested with trypsin. The samples were centrifuged for 10 min at 700  $\times$  g and the cell pellets were resuspended in 300  $\mu$ L MACS buffer (0.5% BSA, 2 mM EDTA, PBS). Dead cells were detected by measuring the fluorescence intensity of PI with a BD FACS Canto 2 (BD Biosciences, Franklin Lakes, NJ, USA). In each case, 3  $\times$  10<sup>4</sup> events were measured and the data were analysed using FlowJo software 10.8.1 (BD Biosciences). Statistical significance was calculated with a paired *t*-test (two-tailed) using GraphPad Prism software (n = 5; \* *p*-value < 0.05, \*\* *p*-value < 0.01, \*\*\* *p*-value < 0.001).

## 2.5. Immunofluorescence

Cells were fixed with 4% paraformaldehyde and were subsequently permeabilised with 0.5% Triton X-100/PBS (Sigma-Aldrich) for 15 min. Prior to incubation with the primary antibodies, blocking with 3% BSA (Sigma-Aldrich) for 1 h at room temperature was performed. Primary antibodies were diluted as follows: anti-mouse KI67 (1:200), anti-rabbit cJUN (1:400) (CST), anti-rabbit phospho-cJUN (1:800) (CST). The plates were then incubated at 4 °C overnight. Labelled cells were detected with the secondary antibodies anti-rabbit Alexa Fluor™ 488 (1:500) (ThermoFisher, Waltham, MA, USA) and anti-mouse Alexa Fluor™ 555 (1:500) (ThermoFisher). Nuclei were stained with Hoechst (1:5000) (ThermoFisher). Pictures were taken under a fluorescence microscope (LSM700; Zeiss, Jena, Germany) and processed with ZenBlue 2012 Software Version 1.1.2.0 (Zeiss) and ImageJ 2.1.0 (NIH).

## 2.6. Western Blotting

Total protein was extracted by lysing the cells with RIPA buffer (Sigma-Aldrich) containing phosphatase and protease inhibitors (Sigma-Aldrich). Protein was quantified with the Pierce's BCA assay kit from Thermo Scientific. Electrophoresis was run with a protein input of 20 µg. Proteins were bound with antibodies including anti-rabbit phospho-SAPK/JNK (1:1000) (CST), anti-rabbit SAPK/JNK (1:1000) (CST), anti-rabbit cJUN (1:1000) (CST), anti-rabbit phospho-cJUN (1:1000) (CST), anti-rabbit SMAD2/3 (1:1000) (CST), anti-rabbit phospho-SMAD2 (CST) (1:1000), anti-rabbit SMAD1 (1:1000) (CST), anti-rabbit phospho-SMAD1/5 (1:1000) (CST), anti-rabbit GPX4 (1:1000) (CST), anti-mouse TFR1 (1:1000) (Invitrogen), anti-rabbit HO-1 (1:2000) (Abcam, Cambridge, UK) and anti-mouse β-actin (1:5000) (CST). The enhanced chemiluminescent (ECL) horseradish peroxidase (HRP) detection technique was used to detect the specific proteins (Life Technologies).

## 2.7. Flow Cytometry-Based Measurement of Lipid Peroxidation

Untreated and JNK-inhibited cells were cultivated for 72 h with daily medium change. For inhibition of ferroptosis, cells were additionally treated with 100 nM Lip-1 (Sigma-Aldrich) 1 h before JNK inhibition via AEG3482. Cells were washed twice with PBS and stained with 1 µM BODIPY<sup>TM</sup> 581/591 C11 (Invitrogen) for 15 min at 37 °C and 5% CO<sub>2</sub>. Subsequently, cells were washed twice with PBS and harvested with trypsin. The samples were centrifuged for 10 min at 700× *g* and resuspended in 300 µL MACS buffer. Lipid peroxidation was detected by measuring the fluorescence intensity of BODIPY 581/591 C11 using BD FACS Canto 2. In each case, 3 × 10<sup>4</sup> events were measured and the data evaluated using FlowJo software. Statistical significance was calculated with an unpaired *t*-test (two-tailed) using GraphPad Prism software (n = 5; \* *p*-value < 0.05, \*\* *p*-value < 0.01, \*\*\* *p*-value < 0.001).

## 2.8. Cell Survival Assay

First, 1 × 10<sup>4</sup> cells per well were seeded in a 96-well plate and treated with 0.1–100 µM erastin (Sigma-Aldrich) at 37 °C and 5% CO<sub>2</sub>. After an incubation of 24 h, CellTiter-Blue<sup>®</sup> (CTB, Promega, Madison, WI, USA) reagent was added to the cells at a ratio of 1:6 with fresh medium and incubated at 37 °C for 1 h. Erastin-treated cells were additionally induced with 10 µM AEG3482 and the combination of 10 µM AEG3482 with 100 nM Lip-1. The change in resazurin absorbance was measured with a Tecan GENios reader (Tecan, Männedorf, Switzerland) at 573 nm. Statistical significance was calculated with an unpaired *t*-test (two-tailed) using GraphPad Prism software (n = 2; \* *p*-value < 0.05, \*\* *p*-value < 0.01, \*\*\* *p*-value < 0.001).

## 2.9. GSH Assay

Following two washing steps with ice-cold PBS, 2 × 10<sup>5</sup> cells were scraped off in 200 µL ice-cold PBS containing 2 mM EDTA. Cell suspensions were lysed with 3% sulfosalicylic acid for 10 min on ice and centrifuged for 10 min at 14,000× *g* and 4 °C. The supernatant was incubated with triethanolamine/H<sub>2</sub>O (1:1) and loaded with assay mix (300 µM DTNB, 450 µM NADPH, 20 units glutathione reductase (Sigma)) on a 96-well plate. A standard curve was generated by measuring different concentrations of pure GSH (Sigma). Absorption was measured at 390 nm for 26 min with a Tecan GENios reader. To determine total protein concentration, pellets were solved in 0.2 N NaOH and incubated overnight at 37 °C and subsequently measured using the bicinchoninic acid (BCA) protein quantification kit (Interchim, Montluçon, France) and BSA as standard. Statistical significance was calculated with a paired *t*-test (two-tailed) using GraphPad Prism software (n = 5; \* *p*-value < 0.05, \*\* *p*-value < 0.01, \*\*\* *p*-value < 0.001).

## 2.10. Seahorse XF Cell Mito Stress Test

Optimal seeding density and FCCP concentration without toxicity response were tested before starting the Seahorse XF Cell Mito Stress Test assay (Agilent, Santa Clara,

CA, USA). A cell density of  $4 \times 10^3$  cells per well and an FCCP concentration of  $2 \mu\text{M}$  were determined and used for the following assays. Cells of the three UdRPC lines, UM51, UM27 and UF21, were seeded on gelatine-coated Seahorse XF Cell Culture Microplates. For mitochondrial oxygen consumption rate (OCR) measurements of JNK pathway inhibition, cells were treated with or without JNK inhibitor AEG3482 for 72 h. Following the manufacturer's protocol, XF sensor cartridges were hydrated with Seahorse XF Calibrant at  $37^\circ\text{C}$  in a hypoxic incubator overnight. The medium was changed to phenol-free Seahorse XF DMEM (10 mM glucose (Sigma Aldrich), 1 mM sodium pyruvate (PAN-Biotech, Aidenbach, Germany) and 2 mM L-glutamine (PAN-Biotech)). The OCR was measured in a Seahorse XFe96 Flux Analyzer with Seahorse Wave 2.4 software (Agilent). In 3 cycles of 3 min of mixing and 3 min of recording,  $1 \mu\text{M}$  oligomycin,  $2 \mu\text{M}$  FCCP and  $0.5 \mu\text{M}$  antimycin/rotenone AA were injected and OCR was measured. The OCR of UF21, UM51 and UM27 was measured with one biological replicate (UM51 and UM27:  $N = 23$ ; UF21:  $N = 46$ ). The data were normalised to the cell number and statistical significance was calculated with an unpaired *t*-test (\* *p*-value < 0.05, \*\* *p*-value < 0.01, \*\*\* *p*-value < 0.001).

### 2.11. TMRM Staining

Cells were seeded on MatTek glass bottom dishes for microscopy followed by a cultivation time of 72 h with or without AEG3482 and daily medium change. Cells were then stained with tetramethylrhodamin (TMRM) and MitoTracker™Green FM (Invitrogen) for 30 min. Briefly, cells were washed thrice with  $1 \times$  PBS and were covered in Opti-MEM™ (Gibco, Billings, MT, USA) without phenol red containing  $10 \mu\text{M}$  HEPES buffer for buffering oxidation of media. Fluorescence imaging of UdRPCs was carried out with a Nikon Ti2 inverted confocal microscope, coupled with an UltraVIEW®VoX spinning disc laser system (PerkinElmer, Waltham, MA, USA) equipped with a 63x oil objective (N.A. 1.2). Imaging was performed in a chamber at  $37^\circ\text{C}$ . For analysis of the fluorescence images, background correction was performed by manually defining a region of interest (ROI) in the background of the image and subtracting the mean fluorescence signal in all images. For each individual cell, a ROI was manually defined for measurement of TMRM fluorescence intensity. Background correction and TMRM intensity measurement of 50 cells per sample were performed with Volocity® software 6.3 for spinning disc microscopy. High variations in fluorescence intensities were cleaned by an outlier test, ROUT ( $Q = 1\%$ ). Cleaned data were used for statistical and graphical analysis, performed in GraphPad Prism software. Statistical significance was calculated with an unpaired *t*-test ( $n = 2$ ; control:  $N = 1$ ; JNK inhibition:  $N = 2$ ; \* *p*-value < 0.05, \*\* *p*-value < 0.01, \*\*\* *p*-value < 0.001).

### 2.12. Quantitative RT-PCR

RNA was isolated with the Directzol RNA MiniPrep kit (Biozol, Eching, Germany) according to the manufacturer's protocol. Subsequently, 500 ng RNA was transcribed to cDNA using MultiScribe Reverse Transcriptase (Life Technologies). Quantitative PCRs were performed in technical triplicates using POWER SYBR Green Master Mix (Life Technologies). Primer sequences are listed in Table S1 (purchased from MWG). Mean values were normalised to the housekeeping gene *RPL37A*, compared to an untreated control for the specific time point and calculated by the  $2^{-\Delta\Delta\text{Ct}}$  method.

### 2.13. Gene Expression Analysis

Total RNA of UdRPCs treated with the JNK inhibitor AEG3482 and untreated cells was hybridised onto microarrays of the Affymetrix Human Clariom S assay at the BMFZ (Biomedizinisches Forschungszentrum) core facility of Heinrich-Heine University, Düsseldorf. The R/Bioconductor environment [23] was employed to process the Affymetrix microarray data. The data were background-corrected via the Bioconductor package oligo [24] and normalised by applying the robust multiarray average (RMA) method. The packages VennDiagram [25] and gplots [26] were used to generate Venn diagrams of the numbers of genes expressed in the control or JNK inhibition conditions. A gene was

considered expressed when the detection  $p$ -value—determined as described in Nguyen et al. (2022)—was below the threshold of 0.05 [27]. Hierarchical clustering was analysed via (i) the R function *hclust* parametrised with Pearson correlation as a similarity measure and complete linkage as an agglomeration method in dendrograms, (ii) the R function *heatmap.2* from the *gplots* package [26], also parametrised with Pearson correlation as a similarity measure and additionally with colour-scaling per row/gene in heatmaps.

#### 2.14. Gene Ontology (GO) and Pathway Analysis

Upregulated genes were calculated by the following criteria: ratio between the JNK-inhibited state and control greater than 1.5 and detection  $p$ -value in the JNK-inhibited state below the threshold of 0.05. Downregulated genes were calculated analogously by the following criteria: ratio between the JNK-inhibited state and control less than 0.67 and detection  $p$ -value in the control state below the threshold of 0.05. From the resulting gene sets, over-represented GOs were determined via the Bioconductor package *GStats* [28]. Kyoto Encyclopedia of Genes and Genomes (KEGG) [29] pathways were analysed for over-representation based on associations between pathways and genes downloaded from the KEGG database in July 2020. For each of the KEGG pathways, the hypergeometric test was applied to the sets of up- and downregulated genes which could be annotated to each pathway. Furthermore, genes from KEGG pathways as well as gene sets found by single cell sequencing analysis of foetal kidney development by Lindström et al. (2018) were employed to generate heatmaps for cluster analysis as described above [30].

#### 2.15. Metascape Analysis

Gene enrichment analyses of differential GO/KEGG terms and biological processes between JNK-inhibited UdRPCs and untreated controls were performed using Metascape (<http://metascape.org/gp/index.html#/main/step1> (accessed on 15 March 2019); Zhou et al. [31]). Exclusive gene sets of JNK inhibition and control of each time point (24 h, 72 h, 120 h) were used as a data source. The Metascape software 3.5 applied hierarchical clustering to display calculated significant GO terms as a tree, which was divided into term clusters with a 0.3 kappa score as a threshold. The top enrichment clusters were represented as heatmaps with a colour scale ranging from grey to dark orange. Statistical significance was therefore displayed in dark orange and lack of enrichment in grey.

### 3. Results

#### 3.1. High Concentrations of JNK Inhibitor Induce Cell Death

Optimal concentrations of the JNK inhibitor AEG3482 were tested on UM51 cells, which were 10  $\mu$ M, 50  $\mu$ M and 100  $\mu$ M. The treatment was conducted for 2 to 5 days with daily medium change. No morphological changes were observed at a concentration of 10  $\mu$ M and the cells were cultivated for up to 5 days before stopping the treatment (Figure S1A). A concentration of 50  $\mu$ M led to a morphology change from the typical rice grain-like appearance to a more flattened appearance with partial detachment and indistinct cell membrane (Figure S1A). The highest dose of 100  $\mu$ M caused complete cell detachment and eventually cell death after 48 h (Figure S1A). UF21 cells treated with 50  $\mu$ M and 100  $\mu$ M JNK inhibitor could be kept for 72 h before the cells died (Figure S1B). As the concentrations of 50  $\mu$ M and 100  $\mu$ M were highly stressful to the cells, a concentration of 10  $\mu$ M AEG3482 was used for all following experiments.

#### 3.2. JNK Inhibition Leads to Decreased Proliferation and Loss of Progenitor State

Cell morphology changes in UM51, UM27 and UF21 cells after JNK inhibition with AEG3482 were observed after 72 h (Figure 1A). In all three cell cultures, JNK inhibition resulted in lower confluency compared to their respective controls. The proliferation capacity of the UdRPCs with and without JNK inhibition at 72 h was analysed by immunofluorescence-based staining for KI67 (Figure 1B). Reduced numbers of KI67<sup>+</sup> proliferative cells were observed under JNK inhibition, which was confirmed by a proliferation



assay displaying the ratio of Ki67<sup>+</sup> cells against the total cell number (Figure 1B,C). An unpaired *t*-test analysis confirmed a highly significant downregulation of Ki67<sup>+</sup> UM51 cells ( $p < 0.001$ ) and significant downregulation in UM27 cells ( $p < 0.05$ ), while there was no significant difference between control and JNK inhibition in UF21 cells (Figure 1C). Moreover, a PI measurement demonstrated a significant increase in cell death upon JNK inhibition in all three UdrPC lines ( $p < 0.01$ ) (Figure 1D). The mRNA expression of progenitor- and cell cycle-related genes was analysed via semi-quantitative real-time PCR. The progenitor markers SIX2, SALL1 and VCAM1 as well as Ki67 were downregulated in JNK-inhibited UM51 and UM27 cells (Figure 1E). Downregulation of VCAM1 and Ki67 was observed in UF21 cells (Figure 1E). A heatmap depicted the expression of *CCND2*, *SMAD4*, *CDC14B*, *HDAC1*, *CCNH*, *WEE1*, *TFDP2* and *RBX1* in the controls, but they were downregulated in JNK-inhibited UM51 cells at the time points of 24 h, 72 h and 120 h (Figure 1F).

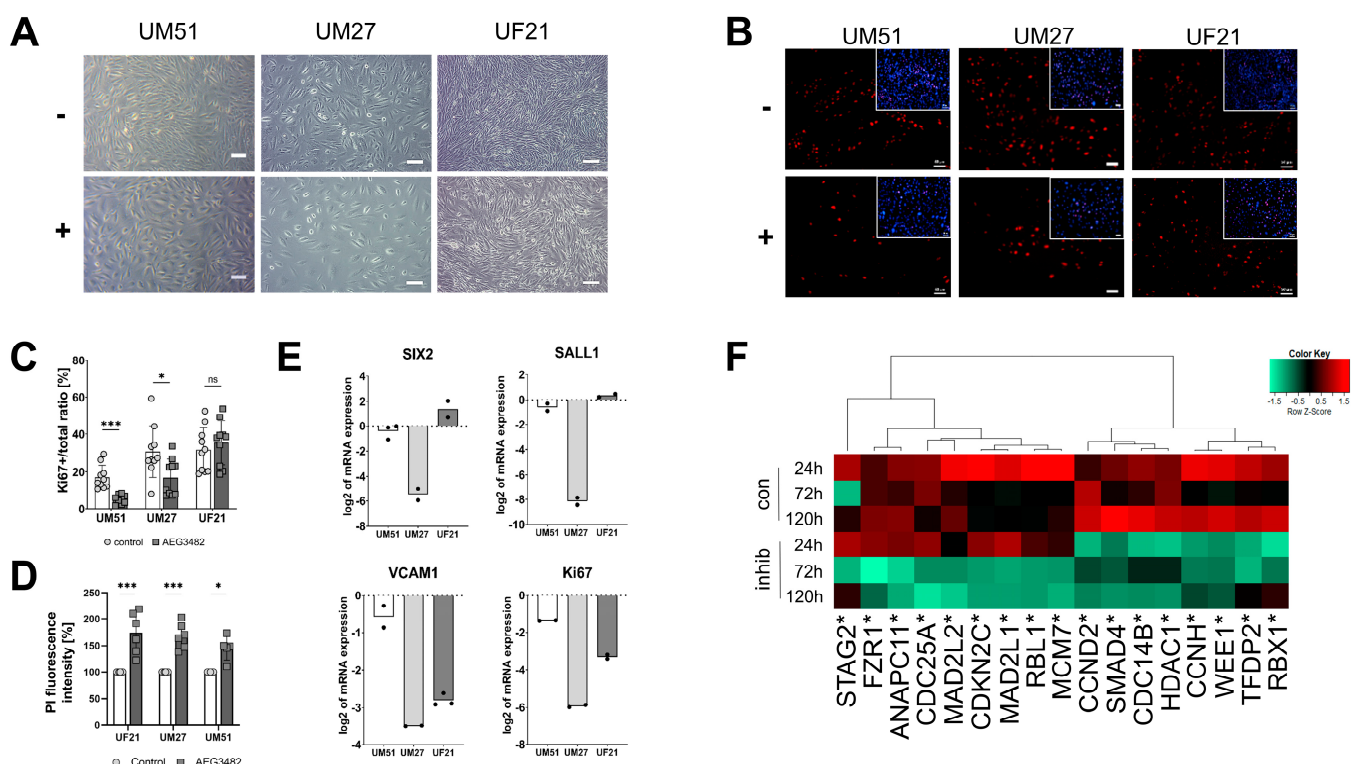


**Figure 1.** Inhibition of JNK reduces the proliferation of UdrPCs. (A) Morphology of the three UdrPCs UM51, UM27 and UF21 with or without AEG3482 treatment after 72 h. Scale bars represent 100  $\mu$ m. (B) Ki67 expression in UdrPCs treated with or not treated with AEG3482 for 72 h. Scale bars represent 50  $\mu$ m. (C) Ki67 proliferation assay for JNK-inhibited UdrPCs ( $n = 10$ ; \*  $p$ -value  $< 0.05$ , \*\*\*  $p$ -value  $< 0.001$ ). (D) Bar graph of PI-measured cell death in JNK-inhibited UdrPCs compared to untreated controls ( $n = 5$ , \*  $p$ -value  $< 0.05$ , \*\*\*  $p$ -value  $< 0.001$ ). Error bars indicate STDEV. (E) mRNA expression of nephron progenitor markers SIX2, SALL1, VCAM1 and Ki67. Mean values were normalised to the housekeeping gene RPL37A. (F) Gene expression of cell cycle-related genes for the time points 24 h, 72 h and 120 h depicted in a Pearson's heatmap.

### 3.3. Cell Cycle-Related Processes Are Regulated by JNK Inhibition

Microarray-based gene expression profiles of UM51 cells treated with JNK inhibitor for an adjusted time span and their specific controls were analysed via transcriptome analysis. A comparison of gene expression between control and JNK inhibition were displayed in Venn diagrams for the time points 24 h, 72 h and 120 h (det  $p > 0.05$ ). Green represents the control, while red denotes JNK inhibition (Figure 2A–C). Complete gene lists for all time points, 24 h, 72 h and 120 h, are listed in Tables S2–S4. Kyoto Encyclopedia of Genes and Genomes (KEGG) pathway analysis was performed using exclusive gene sets pertinent

to control and AEG3482 treatment. Significantly downregulated in all three time points (24 h, 72 h, 120 h) was the KEGG pathway cell cycle (ratio > 1.5) (Table S5). We were able to pinpoint six genes common to all three time points, which we found to be regulated by JNK (*BUB1*, *CCNA2*, *CCNB2*, *CCND2*, *MCM7*, *PLK1*) (Table S5).

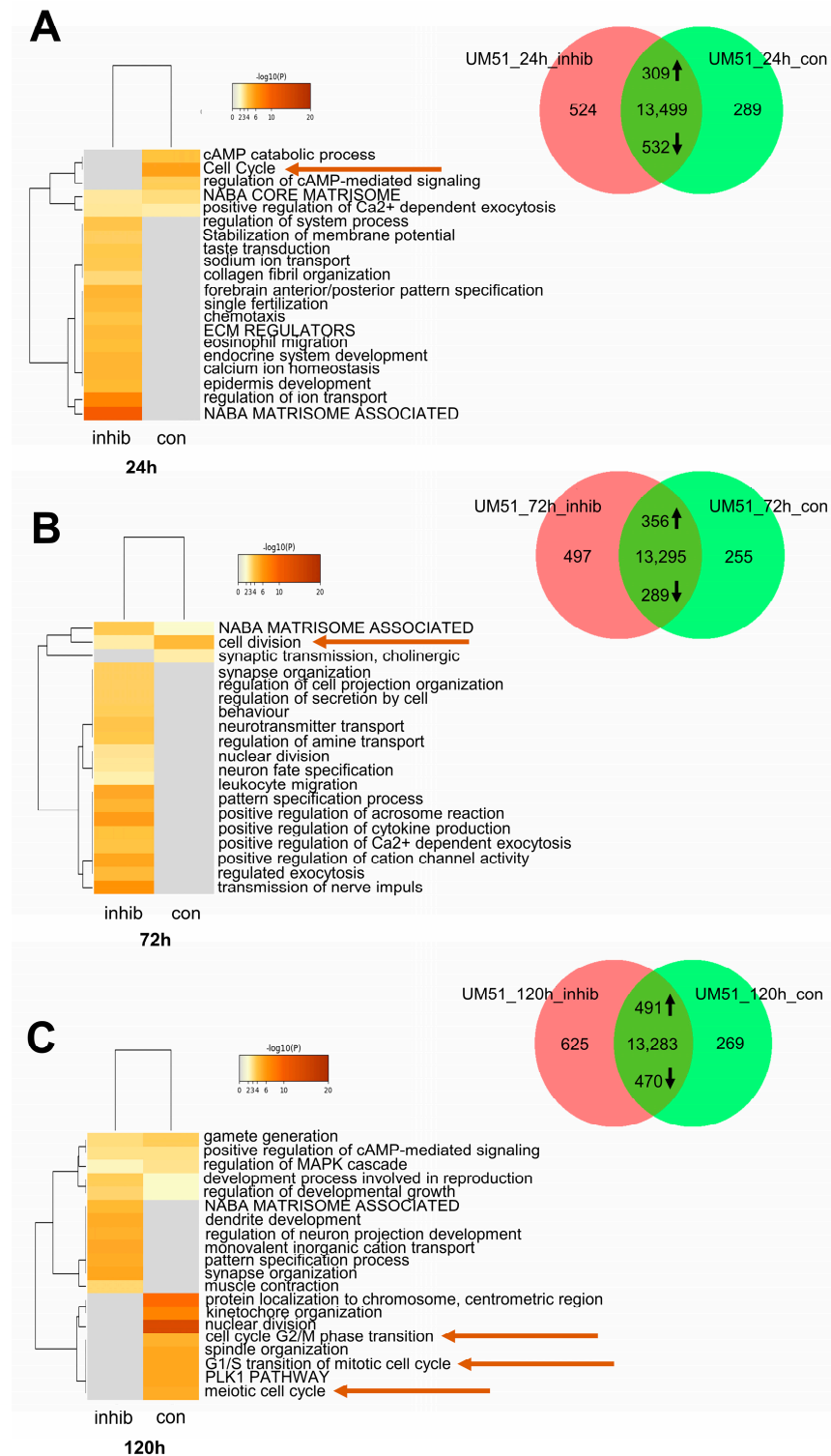


**Figure 2.** JNK signalling is associated with cell cycle processes in UdrPCs. (A) Representative enrichment clusters for control and JNK inhibition after 24 h depicted in a heatmap and cell cycle-related processes marked with an arrow. Venn diagram of control and JNK-inhibited UM51 cells for



the time point 24 h. (B) Representative enrichment clusters for control and JNK inhibition after 72 h depicted in a heatmap and cell cycle-related processes marked with an arrow. Venn diagram of control and JNK-inhibited UM51 cells for the time point 72 h. (C) Representative enrichment clusters for control and JNK inhibition after 120 h depicted in a heatmap and cell cycle-related processes marked with an arrow. Venn diagram of control and JNK-inhibited UM51 cells for the time point 120 h.

Additionally, Metascape-generated enrichment analyses were processed based on the exclusive gene sets in JNK inhibition and control of all three time points (0.3 kappa score). Representative terms of enrichment clusters related to cell cycle and cell division (Table S6) with the highest *p*-values in the UM51 data sets of each time point were represented by heatmaps (Figure 2A–C). Notably, the GO BP terms related to cell cycle lacked enrichment in the JNK inhibitions of 24 h, 72 h and 120 h compared to high enrichment in the specific controls (marked with an arrow in Figure 2A–C).

### 3.4. The Downstream Target Phospho-cJUN Is Downregulated by JNK Inhibition

Next, expression of JNK and downstream target cJUN and its phosphorylated form before and after JNK inhibition was examined (Figure 3A,B). Successful inhibition of JNK phosphorylation by JNK inhibitor AEG3482 was confirmed in all three cell cultures (Figure 3A). Interestingly, the level of p-JNK in treated UF21 cells was less reduced than in the other two cell lines (Figure 3A). The protein level of non-phosphorylated t-JNK was not affected by JNK inhibition (Figure 3A). In addition, siRNA-based transient knockdown of JNK mRNA was tested (Figure S2). A concentration of 1000 ng JNK-siRNA for further use was established via a titration series as the translation of total JNK protein was inhibited by around 30% (Figure S2A–C). In UdrPC lines, UM51 and UM27, a reduced (4–6%) protein level of total JNK was detected (Figure S2D). The protein amount of phosphorylated JNK was reduced by 7–62% in all three UdrPC lines (Figure S2D). On the mRNA level, gene silencing via JNK-siRNA led to downregulation of *MAPK8* (JNK) and *KI67* (Figure S2E). JNK inhibition resulted in a reduced phosphorylation of downstream target cJUN in UM51 and UM27 but not in UF21 cells (Figure 3B). Immunofluorescence-based analysis revealed a lack of differential expression of cJUN and phosphorylated cJUN in untreated and treated UdrPCs (Figure 3C). As our previous study demonstrated the relevance of TGF $\beta$  signalling in the maintenance of self-renewal, protein expression of SMAD2/3 and SMAD1/5 under the influence of JNK inhibition was studied. Interestingly, the level of phosphorylated SMAD1/5 and SMAD2 decreased after JNK inhibition in UM51 and UM27 but not in UF21 cells (Figure 3D). Protein levels of total SMAD2/3 and total SMAD1 were reduced in all three cell cultures (Figure 3D).

### 3.5. UdrPCs Are More Susceptible to Ferroptosis upon JNK Inhibition

KEGG pathway analysis revealed significant upregulation of numerous KEGG pathways, including ferroptosis and glutathione metabolism in JNK-inhibited UM51 cells at all time points (ratio < 0.67) (Table S5B). Following the results of the KEGG analysis, we decided to carry out an in-depth analysis of the ferroptosis pathway. Since lipid peroxidation is a major hallmark of ferroptotic cell death, the accumulation of lipid peroxides was measured in JNK-inhibited UdrPCs (Figure 4A). The cells exhibited a significant increase in lipid peroxidation, indicating increased sensitivity to ferroptosis, which was rescued by the addition of the ferroptosis inhibitor liproxstatin-1 (Lip-1) (Figure 4B). Treatment of the three primary cultures with the ferroptosis-inducing compound erastin demonstrated similar susceptibility to ferroptosis with an IC<sub>50</sub> for erastin in the range of 1 to 3  $\mu$ M (Figure S3A). Treatment with AEG3482 sensitised the UM51 cells even further to erastin-induced ferroptosis (Figure S3B). This effect was rescued by Lip-1 (Figure S3B). In line with JNK inhibition, siRNA-based transient knockdown of JNK increased lipid peroxidation, which was rescued by Lip-1 as well (Figure S3C). JNK inhibition led to an increased level of glutathione (Figure S3D) as well as higher expression of gene sets involved in iron and glutathione metabolism (Figure 4C,D). The findings presented in these heatmaps were verified for

the genes *GLC* and *GLCM* (glutathione metabolism) and *HMOX1*, *SLC11A2* and *TFR1* (iron metabolism) on the mRNA level by qRT-PCR and increased protein level of HO-1 and TFR1 were additionally confirmed by Western blotting (Figure 4E–G). Interestingly, protein expression of the key mediator of lipid peroxides removal, GPX4, did not show any difference between control and JNK inhibition (Figure 4E). Besides the JNK signalling pathway, FGF signalling also plays a role in the self-renewal of UdrPCs. Interestingly, we could also observe a significant increase in lipid peroxidation when FGF signalling was inhibited (Figure S3E).

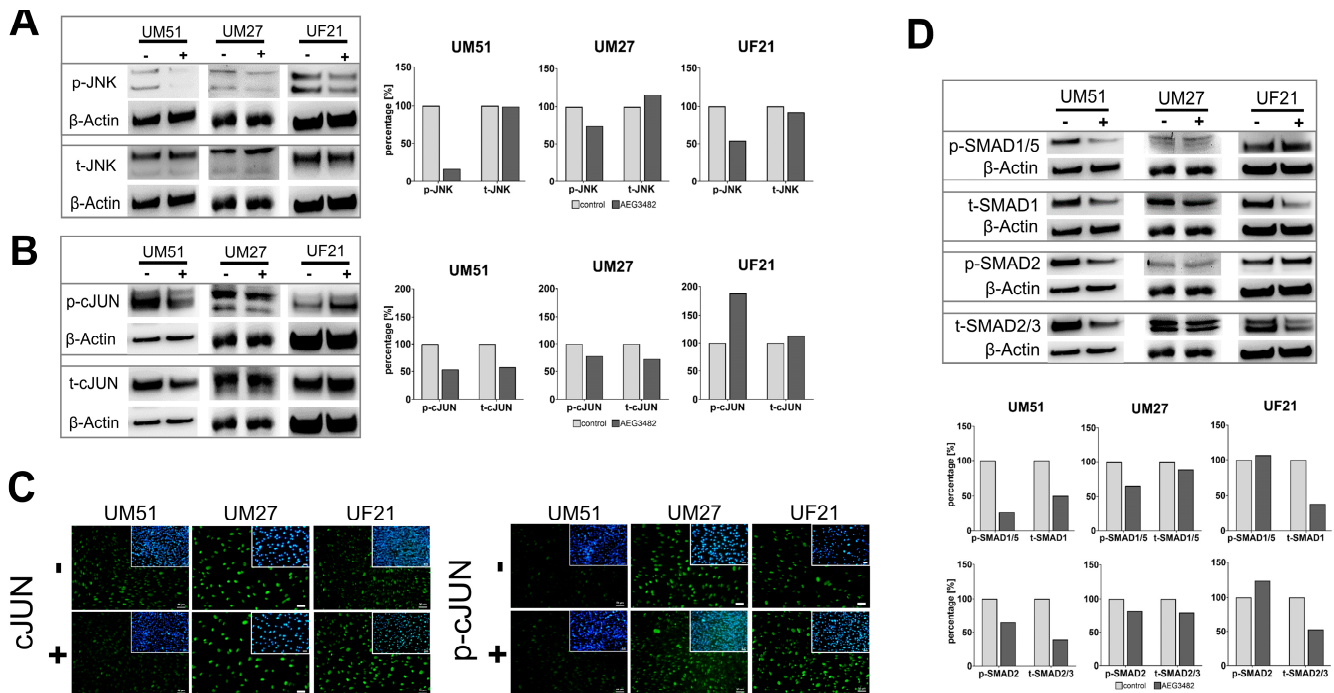


**Figure 3.** Inhibition of JNK signalling affects the downstream target cJUN and SMAD proteins. (A) Representative protein expression (%) of p- and t-JNK in UdrPCs with or without JNK inhibition. (B) Representative protein expression (%) of p- and t-cJUN in UdrPCs with or without JNK inhibition. (C) Immunofluorescence stainings of cJUN and p-cJUN in UdrPCs with or without JNK inhibition. Scale bars represent 50  $\mu$ m. (D) Protein expression of p-/t-SMAD1/5 and p-/t-SMAD2/3 in UdrPCs with or without JNK inhibition.

### 3.6. JNK Inhibition Partially Disrupts the Mitochondrial Membrane Potential and Reduces Respiration

Oxidative phosphorylation in JNK-inhibited and control UdrPCs was evaluated by measuring the oxygen consumption rate (OCR) via a Seahorse Agilent Mito Stress test. The graphs in Figure 5A show basal respiration, the maximal respiratory capacity and the spare respiratory capacity in UdrPCs treated with the JNK inhibitor. The data obtained demonstrate a significant reduction in basal respiration, maximal respiration and spare respiratory capacity in UM51, UM27 and UF21 cells (Figure 5A).

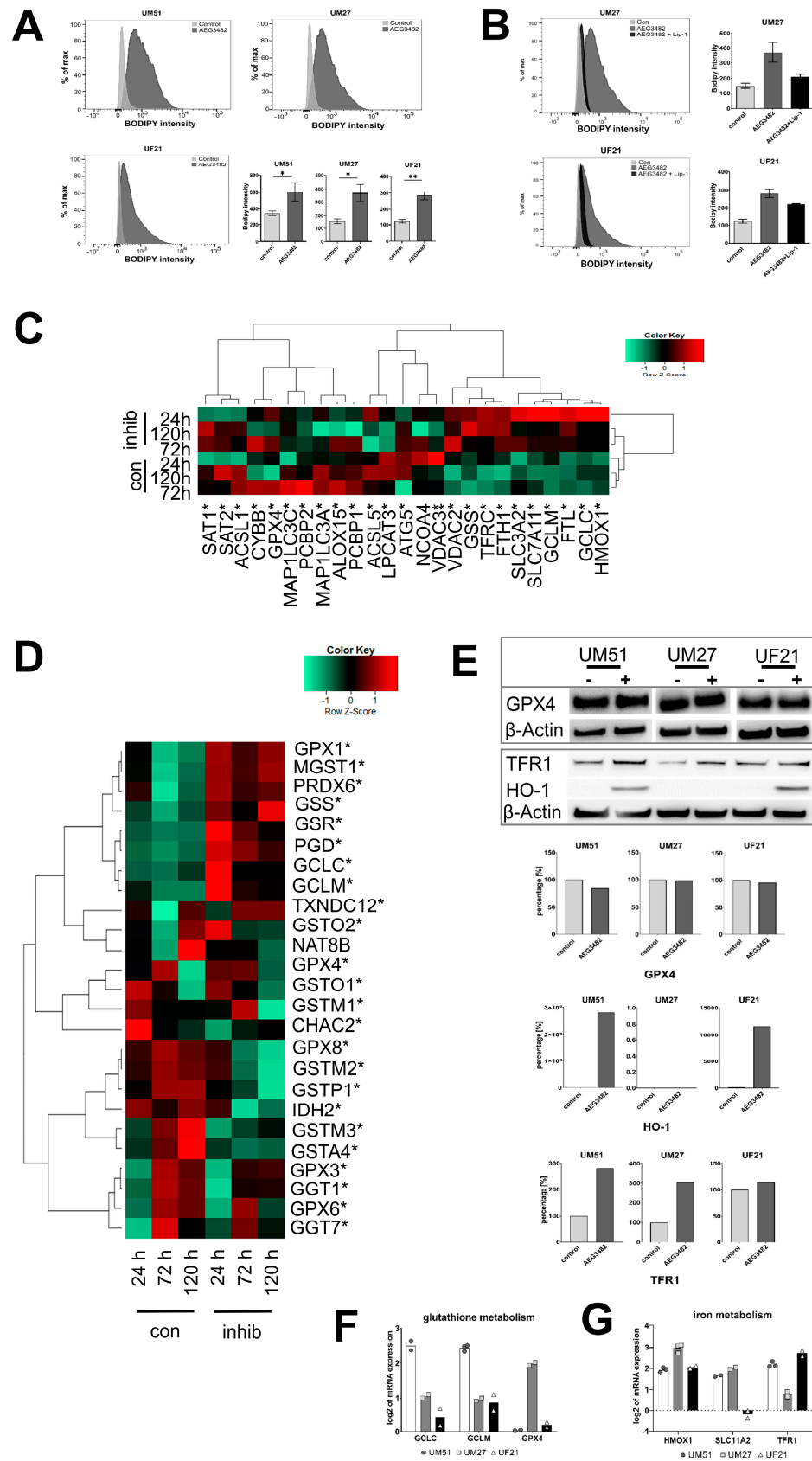


**Figure 4.** Inhibition of JNK signalling increases lipid peroxidation. (A) Representative histograms of measured fluorescence intensities after BODIPY staining and the respective bar plots of mean fluorescence intensity of control or JNK-inhibited UdrPCs (n = 5; \* p-value < 0.05, \*\* p-value < 0.01).

Error bars indicate SEM. **(B)** Representative histograms of measured fluorescence intensities after BODIPY staining and the respective bar plots of mean fluorescence intensity of control, AEG3482 and AEG3482 + Lip-1 ( $n = 5$ ). Error bars indicate SEM. **(C)** Gene expression of iron metabolism-related genes in UM51 cells for the time points 24 h, 72 h and 120 h depicted in a Pearson's heatmap. **(D)** Pearson's heatmap depicting gene expression of glutathione metabolism-related genes in UM51 cells for the time points 24 h, 72 h and 120 h. **(E)** Representative protein expression (%) of GPX4, TFR1 and HO-1 in UdrPCs with or without JNK inhibition. **(F)** mRNA expression of glutathione metabolism-related markers GCLC, GCLM, GPX4. **(G)** mRNA expression of iron metabolism-related markers HMOX1, SLC11A2 and TFR1. Mean values were normalised to the housekeeping gene RPL37A.

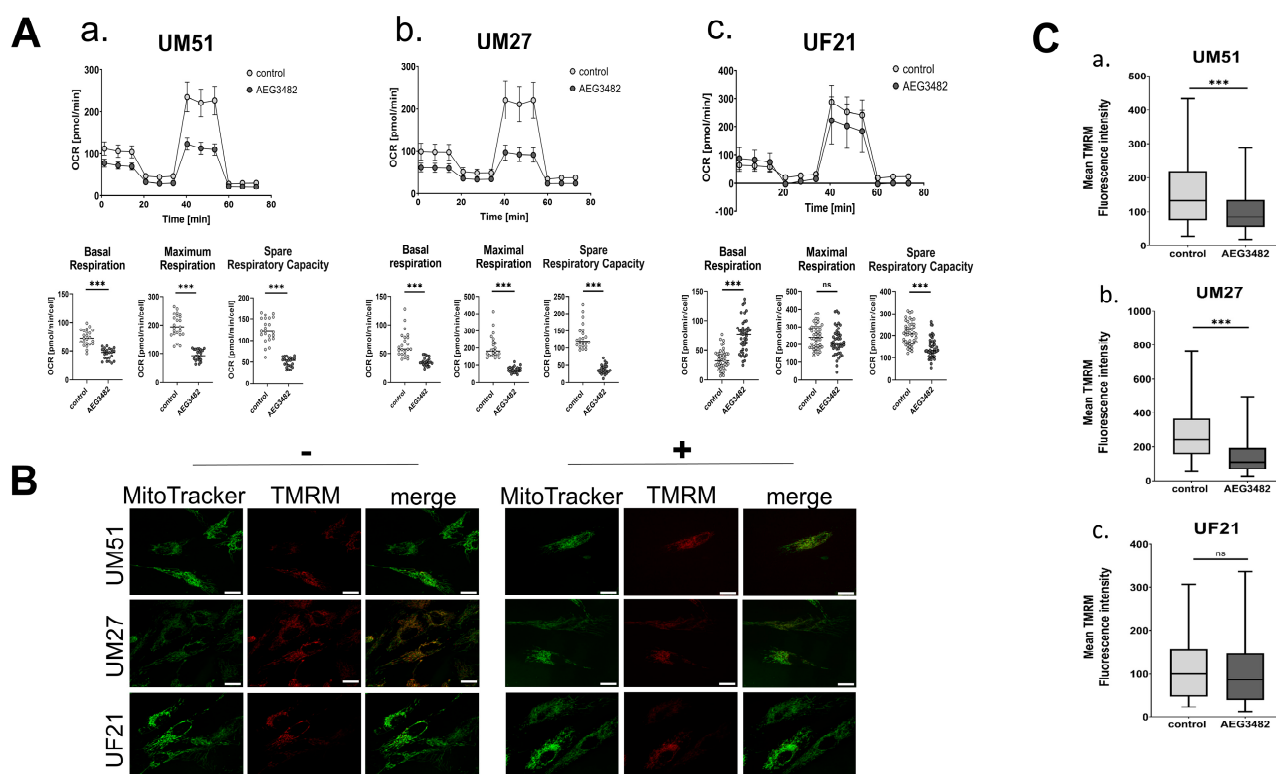


**Figure 5.** JNK signalling regulates mitochondrial respiration via membrane potential. **(A)** Measurement of OCR in real time in UdrPCs. Basal respiration, maximal respiration and spare respiratory capacity are depicted \*\*\*  $p$ -value < 0.001. Error bars indicate SD. **(a)** OCR in UM51 ( $n = 1$ ;  $N = 23$ ). **(b)** OCR in UM27 ( $n = 1$ ;  $N = 23$ ). **(c)** OCR in UF21 ( $n = 1$ ;  $N = 46$ ). **(B)** Fluorescence images of MitoTracker Green and TMRM stainings in UdrPCs UM51, UM27 and UF21 with and without JNK inhibition. Scale bars depict 10  $\mu$ m. **(C)** Measurement of mean TMRM fluorescence signal intensity in UdrPCs \*\*\*  $p$ -value < 0.001. Outliers were removed. Error bars indicate SEM. **(a)** Mean TMRM signal in UM51 is depicted ( $n = 2$ ; ctrl.  $N = 1$ ; +JNK inhibitor  $N = 2$ ). **(b)** Mean TMRM signal in UM27 is depicted ( $n = 2$ ; ctrl.  $N = 1$ ; +JNK inhibitor  $N = 2$ ). Error bars indicate SEM. **(c)** Mean TMRM signal in UF21 is depicted ( $n = 2$ ; ctrl.  $N = 1$ ; +JNK inhibitor  $N = 2$ ).

Reductions of oxidative phosphorylation and SRC are indicators of defective mitochondrial function. Therefore, we investigated the influence of JNK inhibition on mitochondrial membrane potential in UdrPCs via TMRM staining (Figure 5B). We observed a significant reduction of mitochondrial membrane potential in UM51 and UM27 compared to the respective controls (Figure 5C). UF21 cells showed no change in mitochondrial membrane potential upon JNK inhibition (Figure 5C).

## 4. Discussion

### 4.1. JNK Inhibition Decreases the Proliferation and Leads to Loss of Progenitor Character

In this study, JNK signalling was inhibited using the small molecule inhibitor AEG3482 on three UdRPC cultures, UM51, UM27 and UF21. We discovered the importance of JNK for the proliferative potential of the self-renewing urine-derived renal progenitor pool.

Different concentrations of the inhibitor were tested beforehand, and the final concentration of 10  $\mu$ M AEG3482 was used further. Inhibition of the active JNK enzyme was demonstrated by Western blot analysis. The inhibitor did not completely block the phosphorylation of JNK, which would explain why the active form of the direct downstream target cJUN was still observed [8]. Interestingly, in UF21 cells, an inhibitor concentration of 10  $\mu$ M resulted in higher p-cJUN protein levels of treated cells than in non-treated cells. Besides the observation that UF21 cells could tolerate higher concentrations of the JNK inhibitor AEG3482 for longer periods, adaptation or insensitivity to the 10  $\mu$ M concentration of the inhibitor might be an explanation for higher p-cJUN levels. Unlike UM51 and UM27, UF21 cells are from a female donor. Recent studies revealed that gender has an influence on nephrotoxicity, the severity of kidney disease and disease progression [32,33]. Current approaches to determine nephrotoxicity rely on numerous biomarkers and cell death-inducing and metabolic processes [32]. However, these mechanisms are often dependent on age and gender, which could be one of the reasons why UF21 cells had a higher tolerance to the JNK inhibitor AEG3482. Progression of kidney disease is likewise gender-dependent [33]. Lima-Posada et al. observed that male rats had an AKI to CKD transition 4 months after an initial IRI induction, but female rats treated in the same manner did not. Moreover, the removal of ovaries via oophorectomy resulted in a similar outcome of disease progression in female rats to that observed in male rats. This indicates that sex hormones have a reno-protective effect [33].

Even though the cell morphology of the three UdRPC cultures did not change upon JNK inhibition, we observed lower cell density. We detected a significant increase in cell death and assumed a reduced proliferation rate in the AEG3482-treated cells. Comparable results were found in a study on the role of JNK signalling in proliferative nephron progenitors of a mouse model [34]. While it was demonstrated that BMP7 signalling enhanced the proliferation of murine SIX2<sup>+</sup> nephron progenitor cells, JNK inhibition disrupted this effect [34]. It has been shown that BMP7-induced JNK signalling increases the proliferative capacity of SIX2<sup>+</sup> nephron progenitor cells in a mouse model. As UdRPCs share similar characteristics with nephron progenitor cells, a similar outcome regarding the proliferation is very likely. To test the effect of JNK inhibition on the proliferative capacity of UdRPCs, we conducted a follow-up proliferation assay using KI67 as a marker. We could detect a statistically significant reduction of proliferation in UdRPCs, UM51 and UM27, treated with JNK inhibitor, after 72 h. The proliferation rate of JNK-inhibited UF21 cells was not significantly reduced, which might be caused by higher inhibitor tolerance as exhibited before. Moreover, gene expression of KI67 and gene ontologies related to cell cycle were downregulated in JNK-inhibited UdRPCs. In our study, genes of KEGG annotated cell cycle-related GO terms (*BUB1*, *CCNA2*, *CCNB2*, *CCND2*, *MCM7*, *PLK1*) were downregulated by JNK inhibition. The identified common genes are mainly involved in the cell cycle phase transitions, indicating interruption of the cell cycle and subsequent reduction of proliferation. Additionally, a heatmap analysis revealed the absence of cell cycle-related genes (*CCND2*, *SMAD4*, *CDC14B*, *HDAC1*, *CCNH*, *WEE1*, *TFDP2*, *RBX1*) upon JNK inhibition and expression in all controls as well as sustained expression in JNK-inhibited UM51 after 24 h. We observed a downregulation of the progenitor markers *SIX2*, *SALL1* and *VCAM1* (*CD106*) after AEG3482 treatment. Besides the effect of JNK on the proliferative capacity of UdRPCs, reduced expression of the genes *SIX2*, *SALL1* and *CD106* indicates a loss of progenitor status. Muthukrishnan et al. confirmed the Tak1-Jnk-Jun pathway maintained the numbers murine nephron progenitors by keeping the cells in a proliferative state [35]. Therefore, our results signify that JNK signalling is involved in cell cycle progression, proliferation and maintenance of the progenitor state of UdRPCs.



In vivo, NPC self-renewal is sustained by the interaction of growth factors, signalling pathways and metabolic pathways within the nephron progenitor niche and changes can induce differentiation [36,37]. In our previous work, we have observed that FGF-induced TGF $\beta$ /BMP signalling determines the cell fate of urine-derived renal progenitor cells, since we have demonstrated downregulation of p-SMAD2/3 and upregulation of p-SMAD1/5/8 in differentiated UdrPCs upon activation of WNT signalling [2]. We hypothesised that active SMAD2 is necessary to maintain the progenitor state of UdrPCs. In contrast to our previous findings, we observed downregulation of both p-SMAD2 and p-SMAD1/5 upon JNK inhibition. This indicates an interconnection between JNK and SMAD signalling, which is unexpected as SMAD signalling is commonly believed to be independent from JNK signalling [38]. Based on our findings from previous works [2], the decreased expression of p-SMAD2/3 implies the loss of nephron progenitor state due to JNK inhibition. Other signalling pathways such as the BMP7-induced and JNK-independent Smad1/5/8 pathway were also observed to be contributing to the maintenance of the renal progenitor pool in the murine model [39]. Tomita et al. (2013) were able to demonstrate that an inhibition of BMP7-Smad signalling leads to the differentiation of nephron progenitor cells and thus they proposed an important role of BMP7-Smad signalling for the maintenance of the renal progenitor cells and the determination of final nephron numbers [39]. Similar to the mentioned observations in the mouse model, phosphorylated SMAD1/5/8 was decreased in JNK-inhibited UdrPCs UM51 and UM27, indicating the loss of the progenitor state.

#### 4.2. Active JNK Signalling Protects Urine-Derived Renal Progenitor Cells against Ferroptosis

In this study, we have shown that the inhibition of JNK induces ferroptosis. Ferroptosis is characterised by the iron-dependent formation of lipid peroxides leading to cell death. The FACS-based measurement of lipid peroxides confirmed that both JNK inhibition and knockdown increased sensitivity to ferroptosis. Moreover, addition of a ferroptosis inhibitor (liproxstatin-1) protected the cells from accumulating lipid peroxides. The effect of erastin-induced ferroptosis was further increased by addition of AEG3482, which was likewise rescued by Lip-1. FGF signalling regulates the maintenance of self-renewal in NPCs and UdrPCs [2,40]. Inhibition of FGF signalling via FGFR inhibitor SU-5402 increased the level of lipid peroxides significantly. A recent publication described the role of FGF21 in the suppression of iron overload-induced ferroptosis in the liver [41]. Similarly, FGF signalling may have protective properties against ferroptosis in UdrPCs, however, this warrants further investigation beyond the scope of the current study.

KEGG pathway analysis revealed a significant upregulation of genes associated with the GO terms ferroptosis and glutathione metabolism upon JNK inhibition. In our heatmap analyses, we observed clustered expression of ferroptosis-related genes in the JNK-inhibited samples, which are mainly involved in iron and glutathione metabolism. We observed upregulated mRNA expression of glutathione metabolism-related genes *GCLC*, *GCLM* and *SLC7A11* (*cystine-glutamate antiporter X<sub>c</sub><sup>-</sup>*) as well as iron metabolism-related genes *HMOX1*, *SLC11A2* and *TFR1* and a higher protein level of HO-1 and TFR1. Increased expression of regulators of the iron metabolism involved in the iron (Fe<sup>2+</sup>) release from cellular storage and influx of iron can be one of the inducers of ferroptosis [42]. Nevertheless, TFR1 was characterised as a specific marker for ferroptosis [43]. An accumulation of free iron (Fe<sup>2+</sup>) catalyses the Fenton reaction, which generates hydroxyl radicals, thus leading to peroxidation of polyunsaturated fatty acids [44]. Heme oxygenase 1 (HO-1, encoded by *HMOX-1*) could contribute to increased iron levels by liberation of iron during haem degradation [45]. In contrast, other publications describe that HO-1 suppresses ferroptosis. Adedoyin et al. demonstrated increased expression of HO-1 in renal proximal tubular cells which resulted in alleviation of ferroptosis [46]. Moreover, HO-1 is a marker for active NRF2, a transcription factor activating the expression of several genes encoding anti-ferroptotic proteins, including GPX4 [47]. Interestingly, we could not observe a change in the protein level of GPX4 post JNK inhibition. However, upregulated transcript levels of genes encoding proteins important for GSH biosynthesis indicate that the cell has limited

GSH, the essential cofactor for GPX4 activity. High levels of GSH and increased amounts of GPX4 are usually negative regulators of ferroptosis [48], while the opposite induces this form of cell death [49]. Surprisingly, we found increased levels of GSH upon JNK inhibition, although our data imply that JNK inhibition sensitises UdrPCs to ferroptosis. The combination of higher GSH levels and constant GPX4 levels might suggest that JNK signalling acts via GSH-independent ferroptotic pathways such as FSP1 [50].

Ferroptosis was discovered to be one of the causes in the induction of kidney diseases such as acute kidney injury, I/R injury, clear cell renal cell carcinoma and adrenocortical carcinomas [17]. Therefore, we assume that UdrPCs treated with the JNK inhibitor AEG3482 may represent an easily available model for studying ferroptosis-induced kidney diseases in the near future.

#### *4.3. JNK Signalling Is Involved in the Metabolic Activity Associated with the Maintenance of Self-Renewal in UdrPCs*

The role of mitochondria in ferroptosis is not currently understood [19]. Mitochondria could promote ferroptosis via formation of peroxides by altered electron transfer during oxidative phosphorylation but could also be a target of ferroptosis by inducing damage to mitochondrial membranes, leading to dysfunctional energy metabolism. Since JNK inhibition is accompanied by ferroptosis, we decided to study the respiratory function of mitochondria in JNK-inhibited UdrPCs. Therefore, a Mito Stress test was performed to determine the influence of JNK inhibition on mitochondrial respiration in UdrPCs. We observed a significant reduction of mitochondrial respiration in UdrPCs upon JNK inhibition. In particular, the spare respiratory capacity (SRC) is an indicator of cellular health, since it represents the cell's ability to react to increased energy demand or stress. Therefore, significant reduction of the SRC in all three UdrPC cultures demonstrates a loss of metabolic capacity of mitochondria upon inhibition of JNK signalling.

Oxidative phosphorylation is crucially dependent on the membrane potential generated by the electron transport chain (ETC) in the inner mitochondrial membrane [51]. Thus, malfunction of the ETC in mitochondria is usually accompanied by the loss of mitochondrial membrane potential [52]. We performed TMRM staining to investigate if there is a link between the reduction OCR and a disruption of mitochondrial membrane potential caused by JNK inhibition. With TMRM staining, we could indeed observe a reduction in mitochondrial membrane potential upon JNK inhibition. Overall, there is evidence that mitochondrial dysfunction is increased by JNK pathway inhibition in UdrPCs.

JNK signalling is involved in proliferation processes and, consequently, this pathway also regulates cellular respiration. Xie, Sun et al. demonstrated that inhibiting the JNK signalling pathway in haematopoietic stem cells results in a reduction in the expression of genes related to oxidative phosphorylation [53]. Our data indicate that inhibition of the JNK signalling pathway leads to mitochondrial impairment and ferroptosis. The hallmarks for iron-dependent cell death include morphological changes of the mitochondria such as a blistered cell membrane, reduction in size and loss of mitochondrial cristae [15, 17]. Since mitochondrial complexes involved in oxidative phosphorylation are localised in the inner mitochondrial membrane, ferroptosis-related damage of mitochondria may be an explanation for the rupture of the mitochondrial membrane and thus impaired oxidative phosphorylation [54]. Moreover, mitochondrial dysfunction via mitochondrial ROS production activates mitochondrial JNK signalling, which promotes Bax-dependent apoptosis [55,56]. Based on this finding, JNK inhibition in our study could lead to an inhibition of Bax-dependent apoptosis, which simultaneously enhances ferroptosis.

## **5. Conclusions**

In this study, we demonstrated the importance of JNK signalling for the maintenance of self-renewal and the proliferation capacity of SIX2-positive urine-derived renal progenitor cells. JNK pathway inhibition led to the emergence of ferroptosis-induced cell death in UdrPCs and was accompanied by disrupted mitochondrial membrane potential and

overall reduced oxidative phosphorylation. We therefore propose JNK signalling as a potential target for studying ferroptosis during nephrogenesis and kidney-associated diseases.

**Supplementary Materials:** The following supporting information can be downloaded at: <https://www.mdpi.com/article/10.3390/cells12172197/s1>, Figure S1: Cell morphology of UdRPCs after treatment with different concentrations of AEG3482 (related to Figure 1); Figure S2: siRNA inhibition of JNK induces ferroptosis (related to Figure 4); Figure S3: JNK inhibition amplifies the effect of erastin-induced ferroptosis (related to Figure 4); Table S1: List of qRT-PCR primers (related to Figures 1 and 4); Table S2: Lists of exclusive and common genes of the Venn analysis for 24 h (related to Figure 2); Table S3: Lists of exclusive and common genes of the Venn analysis for 72 h (related to Figure 2); Table S4: Lists of exclusive and common genes of the Venn analysis for 120 h (related to Figure 2); Table S5: GO terms of down- and upregulated genes from KEGG analysis for the time points 24 h, 72 h and 120 h after JNK inhibition (related to Figure 2); Table S6: Downregulated cell cycle-related gene lists of Metascape analysis for the time points 24 h, 72 h and 120 h after JNK inhibition (related to Figure 2).

**Author Contributions:** L.N. designed and performed experiments, analysed the data and wrote and edited the manuscript. M.W. and L.T. assisted in experimental design, performed experiments, analysed data and wrote and edited the manuscript. W.W. prepared the formal analysis, carried out data curation, helped with the figures and edited the manuscript. A.S.R. supervised oxidative phosphorylation-related experiments and edited the manuscript. C.B. supervised ferroptosis-related experiments and edited the manuscript. J.A. conceptualised the work, wrote and edited the manuscript, carried out project administration, acquired funding and supervised the study. All authors have read and agreed to the published version of the manuscript.

**Funding:** J.A. acknowledges the medical faculty of Heinrich Heine University for financial support. J.A., C.B. and A.S.R. acknowledge that this work is partly funded by the Deutsche Forschungsgemeinschaft (DFG, German Research Foundation)—417677437/GRK2578.

**Institutional Review Board Statement:** Not applicable.

**Informed Consent Statement:** Not applicable.

**Data Availability Statement:** Microarray raw data have been deposited at NCBI GEO and are publicly available as of the date of publication. Accession number is listed in the key resources table. All data reported in this paper will be shared by the corresponding author upon request. Any additional information required to reanalyse the data reported in this paper is available from the corresponding author upon request.

**Conflicts of Interest:** The authors declare no conflict of interest.

## References

1. Oliveira Arcolino, F.; Tort Piella, A.; Papadimitriou, E.; Bussolati, B.; Antonie, D.J.; Murray, P.; Van Den Heuvel, L.; Levchenko, E. Human urine as a noninvasive source of kidney cells. *Stem Cells Int.* **2015**, *2015*, 362562. [[CrossRef](#)] [[PubMed](#)]
2. Rahman, M.S.; Wruck, W.; Spitzhorn, L.S.; Nguyen, L.; Bohndorf, M.; Martins, S.; Asar, F.; Ncube, A.; Erichsen, L.; Graffmann, N.; et al. The FGF, TGF $\beta$  and WNT axis Modulate Self-renewal of Human SIX2+ Urine Derived Renal Progenitor Cells. *Sci. Rep.* **2020**, *10*, 739. [[CrossRef](#)] [[PubMed](#)]
3. Sato, M.; Takizawa, H.; Nakamura, A.; Turner, B.J.; Shabanpoor, F.; Aoki, Y. Application of Urine-Derived Stem Cells to Cellular Modeling in Neuromuscular and Neurodegenerative Diseases. *Front. Mol. Neurosci.* **2019**, *12*, 297. [[CrossRef](#)] [[PubMed](#)]
4. Pavathuparambil Abdul Manaph, N.; Al-Hawaas, M.; Bobrovskaya, L.; Coates, P.T.; Zhou, X.F. Urine-derived cells for human cell therapy. *Stem Cell Res. Ther.* **2018**, *9*, 189. [[CrossRef](#)] [[PubMed](#)]
5. Zhang, D.; Wei, G.; Li, P.; Zhou, X.; Zhang, Y. Urine-derived stem cells: A novel and versatile progenitor source for cell-based therapy and regenerative medicine. *Genes Dis.* **2014**, *1*, 8–17. [[CrossRef](#)] [[PubMed](#)]
6. Bharadwaj, S.; Liu, G.; Shi, Y.; Wu, R.; Yang, B.; He, T.; Fan, Y.; Lu, X.; Zhou, X.; Liu, H.; et al. Multipotential differentiation of human urine-derived stem cells: Potential for therapeutic applications in urology. *Stem Cells* **2013**, *31*, 1840–1856. [[CrossRef](#)]
7. Erichsen, L.; Thimm, C.; Bohndorf, M.; Rahman, M.S.; Wruck, W.; Adjaye, J. Activation of the Renin–Angiotensin System Disrupts the Cytoskeletal Architecture of Human Urine-Derived Podocytes. *Cells* **2022**, *11*, 1095. [[CrossRef](#)]
8. Javelaud, D.; Mauviel, A. Crosstalk mechanisms between the mitogen-activated protein kinase pathways and Smad signaling downstream of TGF- $\beta$ : Implications for carcinogenesis. *Oncogene* **2005**, *24*, 5742–5750. [[CrossRef](#)]

9. Awazu, M. Mitogen-activated Protein Kinases in the Development of Normal and Diseased Kidneys. *Child Kidney Dis* **2017**, *21*, 1–7. [[CrossRef](#)]
10. Engel, M.E.; McDonnell, M.A.; Law, B.K.; Moses, H.L. Interdependent SMAD and JNK Signaling in Transforming Growth Factor- $\beta$ -mediated Transcription. *J. Biol. Chem.* **1999**, *274*, 37413–37420. [[CrossRef](#)]
11. Tournier, C.; Hess, P.; Yang, D.D.; Xu, J.; Turner, T.K.; Nimmual, A.; Bar-Sagi, D.; Jones, S.N.; Flavell, R.A.; Davis, R.J. Requirement of JNK for stress-induced activation of the cytochrome c-mediated death pathway. *Science* **2000**, *288*, 870–874. [[CrossRef](#)] [[PubMed](#)]
12. Smith, A.O.; Jonassen, J.A.; Preval, K.M.; Davis, R.J.; Pazour, G.J. RESEARCH ARTICLE c-Jun N-terminal kinase (JNK) signaling contributes to cystic burden in polycystic kidney disease. *PLoS Genet.* **2021**, *17*, e1009711. [[CrossRef](#)] [[PubMed](#)]
13. Tang, S.; Xiao, X. Ferroptosis and kidney diseases. *Int. Urol. Nephrol.* **2020**, *52*, 497–503. [[CrossRef](#)] [[PubMed](#)]
14. Dixon, S.J.; Lemberg, K.M.; Lamprecht, M.R.; Skouta, R.; Zaitsev, E.M.; Gleason, C.E.; Patel, D.N.; Bauer, A.J.; Cantley, A.M.; Yang, W.S.; et al. Ferroptosis: An iron-dependent form of nonapoptotic cell death. *Cell* **2012**, *149*, 1060–1072. [[CrossRef](#)]
15. Li, J.; Cao, F.; Yin, H.; Huang, Z.; Lin, Z.; Mao, N.; Sun, B.; Wang, G. Ferroptosis: Past, present and future. *Cell Death Dis.* **2020**, *11*, 88. [[CrossRef](#)]
16. Hu, Z.; Zhang, H.; Yang, S.; Wu, X.; He, D.; Cao, K.; Zhang, W. Emerging Role of Ferroptosis in Acute Kidney Injury. *Oxid. Med. Cell. Longev.* **2019**, *2019*, 8010614. [[CrossRef](#)] [[PubMed](#)]
17. Galluzzi, L.; Vitale, I.; Aaronson, S.A.; Abrams, J.M.; Adam, D.; Agostinis, P.; Alnemri, E.S.; Altucci, L.; Amelio, I.; Andrews, D.W.; et al. Molecular mechanisms of cell death: Recommendations of the Nomenclature Committee on Cell Death 2018. *Cell Death Differ.* **2018**, *25*, 486–541. [[CrossRef](#)]
18. Ingold, I.; Berndt, C.; Schmitt, S.; Doll, S.; Poschmann, G.; Buday, K.; Roveri, A.; Peng, X.; Porto Freitas, F.; Seibt, T.; et al. Selenium Utilization by GPX4 Is Required to Prevent Hydroperoxide-Induced Ferroptosis. *Cell* **2018**, *172*, 409–422.e21. [[CrossRef](#)]
19. Jiang, X.; Stockwell, B.R.; Conrad, M. Ferroptosis: Mechanisms, biology and role in disease. *Nat. Rev. Mol. Cell Biol.* **2021**, *22*, 266–282. [[CrossRef](#)]
20. Conrad, M.; Lorenz, S.M.; Proneth, B. Targeting Ferroptosis: New Hope for As-Yet-Incurable Diseases. *Trends Mol. Med.* **2021**, *27*, 113–122. [[CrossRef](#)]
21. Friedmann Angeli, J.P.; Schneider, M.; Proneth, B.; Tyurina, Y.Y.; Tyurin, V.A.; Hammond, V.J.; Herbach, N.; Aichler, M.; Walch, A.; Eggenhofer, E.; et al. Inactivation of the ferroptosis regulator Gpx4 triggers acute renal failure in mice. *Nat. Cell Biol.* **2014**, *16*, 1180–1191. [[CrossRef](#)] [[PubMed](#)]
22. Tonnus, W.; Meyer, C.; Steinebach, C.; Belavgeni, A.; von Mässenhausen, A.; Gonzalez, N.Z.; Maremonti, F.; Gembardt, F.; Himmerkus, N.; Latk, M.; et al. Dysfunction of the key ferroptosis-surveilling systems hypersensitizes mice to tubular necrosis during acute kidney injury. *Nat. Commun.* **2021**, *12*, 4402. [[CrossRef](#)] [[PubMed](#)]
23. Gentleman, R.C.; Carey, V.J.; Bates, D.M.; Bolstad, B.; Dettling, M.; Dudoit, S.; Ellis, B.; Gautier, L.; Ge, Y.; Gentry, J.; et al. Bioconductor: Open software development for computational biology and bioinformatics. *Genome Biol.* **2004**, *5*, R80. [[CrossRef](#)] [[PubMed](#)]
24. Carvalho, B.S.; Irizarry, R.A. A framework for oligonucleotide microarray preprocessing. *Bioinformatics* **2010**, *26*, 2363–2367. [[CrossRef](#)] [[PubMed](#)]
25. Chen, H.; Boutros, P.C. VennDiagram: A package for the generation of highly-customizable Venn and Euler diagrams in R. *BMC Bioinform.* **2011**, *12*, 35. [[CrossRef](#)] [[PubMed](#)]
26. Warnes, G.; Bolker, B.; Bonebakker, L.; Gentleman, R.; Huber, W.; Liaw, A.; Lumley, T.; Mächler, M.; Magnusson, A.; Möller, S. *gplots: Various R Programming Tools for Plotting Data*; R Core Team: Vienna, Austria, 2005; Volume 2.
27. Nguyen, L.; Wruck, W.; Erichsen, L.; Graffmann, N.; Adjaye, J. The Nephrotoxin Puromycin Aminonucleoside Induces Injury in Kidney Organoids Differentiated from Induced Pluripotent Stem Cells. *Cells* **2022**, *11*, 635. [[CrossRef](#)]
28. Falcon, S.; Gentleman, R. Using GOstats to test gene lists for GO term association. *Bioinformatics* **2007**, *23*, 257–258. [[CrossRef](#)]
29. Kanehisa, M.; Furumichi, M.; Tanabe, M.; Sato, Y.; Morishima, K. KEGG: New perspectives on genomes, pathways, diseases and drugs. *Nucleic Acids Res.* **2017**, *45*, D353–D361. [[CrossRef](#)]
30. Lindström, N.O.; De Sena Brandine, G.; Tran, T.; Ransick, A.; Suh, G.; Guo, J.; Kim, A.D.; Parvez, R.K.; Ruffins, S.W.; Rutledge, E.A.; et al. Progressive Recruitment of Mesenchymal Progenitors Reveals a Time-Dependent Process of Cell Fate Acquisition in Mouse and Human Nephrogenesis. *Dev. Cell* **2018**, *45*, 651–660. [[CrossRef](#)]
31. Zhou, Y.; Zhou, B.; Pache, L.; Chang, M.; Khodabakhshi, A.H.; Tanaseichuk, O.; Benner, C.; Chanda, S.K. Metascape provides a biologist-oriented resource for the analysis of systems-level datasets. *Nat. Commun.* **2019**, *10*, 1523. [[CrossRef](#)]
32. Barnett, L.M.A.; Cummings, B.S. Nephrotoxicity and Renal Pathophysiology: A Contemporary Perspective. *Toxicol. Sci.* **2018**, *164*, 379–390. [[CrossRef](#)]
33. Lima-Posada, I.; Portas-Cortés, C.; Pérez-Villalva, R.; Fontana, F.; Rodríguez-Romo, R.; Prieto, R.; Sánchez-Navarro, A.; Rodríguez-González, G.L.; Gamba, G.; Zambrano, E.; et al. Gender Differences in the Acute Kidney Injury to Chronic Kidney Disease Transition. *Sci. Rep.* **2017**, *7*, 12270. [[CrossRef](#)] [[PubMed](#)]
34. Blank, U.; Brown, A.; Adams, D.C.; Karolak, M.J.; Oxburgh, L. BMP7 promotes proliferation of nephron progenitor cells via a JNK-dependent mechanism. *Development* **2009**, *136*, 3557–3566. [[CrossRef](#)] [[PubMed](#)]
35. Muthukrishnan, S.D.; Yang, X.; Friesel, R.; Oxburgh, L. Concurrent BMP7 and FGF9 signalling governs AP-1 function to promote self-renewal of nephron progenitor cells. *Nat. Commun.* **2015**, *6*, 10027. [[CrossRef](#)]



36. Liu, J.; Edgington-Giordano, F.; Dugas, C.; Abrams, A.; Katakam, P.; Satou, R.; Saifudeen, Z. Regulation of Nephron Progenitor Cell Self-Renewal by Intermediary Metabolism. *J. Am. Soc. Nephrol.* **2017**, *28*, 3323–3335. [[CrossRef](#)] [[PubMed](#)]
37. Oxburgh, L.; Rosen, C.J. New Insights into Fuel Choices of Nephron Progenitor Cells. *J. Am. Soc. Nephrol.* **2017**, *28*, 3133–3135. [[CrossRef](#)] [[PubMed](#)]
38. Zhang, Y.E. Non-Smad pathways in TGF-beta signaling. *Cell Res.* **2009**, *19*, 128–139. [[CrossRef](#)]
39. Tomita, M.; Asada, M.; Asada, N.; Nakamura, J.; Oguchi, A.; Higashi, A.Y.; Endo, S.; Robertson, E.; Kimura, T.; Kita, T.; et al. Bmp7 Maintains Undifferentiated Kidney Progenitor Population and Determines Nephron Numbers at Birth. *PLoS ONE* **2013**, *8*, e73554. [[CrossRef](#)]
40. Barak, H.; Huh, S.-H.; Chen, S.; Jeanpierre, C.; Martinovic, J.; Parisot, M.; Bole-Feysot, C.; Nitschké, P.; Salomon, R.; Antignac, C.; et al. FGF9 and FGF20 Maintain the Stemness of Nephron Progenitors in Mice and Man. *Dev. Cell* **2012**, *22*, 1191–1207. [[CrossRef](#)]
41. Wu, A.; Feng, B.; Yu, J.; Yan, L.; Che, L.; Zhuo, Y.; Luo, Y.; Yu, B.; Wu, D.; Chen, D. Fibroblast growth factor 21 attenuates iron overload-induced liver injury and fibrosis by inhibiting ferroptosis. *Redox Biol.* **2021**, *46*, 102131. [[CrossRef](#)]
42. Chen, X.; Yu, C.; Kang, R.; Tang, D. Iron Metabolism in Ferroptosis. *Front. Cell Dev. Biol.* **2020**, *8*, 590226. [[CrossRef](#)] [[PubMed](#)]
43. Feng, H.; Schorpp, K.; Jin, J.; Yozwiak, C.E.; Hoffstrom, B.G.; Decker, A.M.; Rajbhandari, P.; Stokes, M.E.; Bender, H.G.; Csuka, J.M.; et al. Transferrin Receptor Is a Specific Ferroptosis Marker. *Cell Rep.* **2020**, *30*, 3411–3423.e7. [[CrossRef](#)] [[PubMed](#)]
44. Latunde-Dada, G.O. Ferroptosis: Role of lipid peroxidation, iron and ferritinophagy. *Biochim. Biophys. Acta-Gen. Subj.* **2017**, *1861*, 1893–1900. [[CrossRef](#)]
45. Kwon, M.Y.; Park, E.; Lee, S.J.; Chung, S.W. Heme oxygenase-1 accelerates erastin-induced ferroptotic cell death. *Oncotarget* **2015**, *6*, 24393–24403. [[CrossRef](#)] [[PubMed](#)]
46. Adedoyin, O.; Boddu, R.; Traylor, A.; Lever, J.M.; Bolisetty, S.; George, J.F.; Agarwal, A. Heme oxygenase-1 mitigates Ferroptosis in renal proximal tubule cells. *Am. J. Physiol.-Ren. Physiol.* **2018**, *314*, F702–F714. [[CrossRef](#)] [[PubMed](#)]
47. Nishizawa, H.; Yamanaka, M.; Igarashi, K. Ferroptosis: Regulation by competition between NRF2 and BACH1 and propagation of the death signal. *FEBS J.* **2022**, *290*, 1688–1704. [[CrossRef](#)]
48. Sharma, A.; Jeet, S.; Flora, S. Review Article Positive and Negative Regulation of Ferroptosis and Its Role in Maintaining Metabolic and Redox Homeostasis. *Oxidative Med. Cell. Longev.* **2021**, *2021*, 9074206. [[CrossRef](#)]
49. Berndt, C.; Lillig, C.H. Glutathione, Glutaredoxins, and Iron. *Antioxidants Redox Signal.* **2017**, *27*, 1235–1251. [[CrossRef](#)]
50. Doll, S.; Freitas, F.P.; Shah, R.; Aldrovandi, M.; da Silva, M.C.; Ingold, I.; Goya Grocin, A.; Xavier da Silva, T.N.; Panzilius, E.; Scheel, C.H.; et al. FSP1 is a glutathione-independent ferroptosis suppressor. *Nature* **2019**, *575*, 693–698. [[CrossRef](#)] [[PubMed](#)]
51. Perry, S.W.; Norman, J.P.; Barbieri, J.; Brown, E.B.; Gelbard, H.A. Mitochondrial membrane potential probes and the proton gradient: A practical usage guide. *Biotechniques* **2011**, *50*, 98–115. [[CrossRef](#)]
52. van der Stel, W.; Yang, H.; le Dévédec, S.E.; van de Water, B.; Beltman, J.B.; Danen, E.H.J. High-content high-throughput imaging reveals distinct connections between mitochondrial morphology and functionality for OXPHOS complex I, III, and V inhibitors. *Cell Biol. Toxicol.* **2022**, *39*, 415–433. [[CrossRef](#)] [[PubMed](#)]
53. Xie, H.; Sun, Z.; Xiao, X.; Liu, D.; Qi, H.; Tian, G.; Chen, M.; Chen, L.; Su, X. Transient Inhibition of the JNK Pathway Promotes Human Hematopoietic Stem Cell Quiescence and Engraftment. *Stem Cells Transl. Med.* **2022**, *11*, 597–603. [[CrossRef](#)] [[PubMed](#)]
54. Nolfi-Donegan, D.; Braganza, A.; Shiva, S. Mitochondrial electron transport chain: Oxidative phosphorylation, oxidant production, and methods of measurement. *Redox Biol.* **2020**, *37*, 101674. [[CrossRef](#)]
55. Chambers, J.W.; LoGrasso, P.V. Mitochondrial c-Jun N-terminal Kinase (JNK) signaling initiates physiological changes resulting in amplification of reactive oxygen species generation. *J. Biol. Chem.* **2011**, *286*, 16052–16062. [[CrossRef](#)] [[PubMed](#)]
56. Niizuma, K.; Endo, H.; Chan, P.H. Oxidative stress and mitochondrial dysfunction as determinants of ischemic neuronal death and survival. *J. Neurochem.* **2010**, *109*, 133–138. [[CrossRef](#)] [[PubMed](#)]

**Disclaimer/Publisher’s Note:** The statements, opinions and data contained in all publications are solely those of the individual author(s) and contributor(s) and not of MDPI and/or the editor(s). MDPI and/or the editor(s) disclaim responsibility for any injury to people or property resulting from any ideas, methods, instructions or products referred to in the content.